

Article

Research on Capacity Configuration for Green Power Substitution in an Isolated Grid Containing Electrolytic Aluminum

Min You ¹, Yunguang Wang ², Haiyun Wang ^{1,*}, Aisikaer Wusiman ² and Liangnian Lv ²

¹ Engineering Research Center of Education Ministry for Renewable Energy Power Generation and Grid Connection, Xinjiang University, Urumqi 830017, China; 107552101428@stu.xju.edu.cn

² Goldwind Science & Technology Co., Ltd., Beijing 100176, China; wangyunguang@goldwind.com (Y.W.); dkbaskr@goldwind.com (A.W.); lvliangnian@goldwind.com (L.L.)

* Correspondence: why@xju.edu.cn

Abstract: The deployment of a green power alternative within an isolated network, powered by renewable energy sources, in the “Three North” region of China can facilitate the substitution of high-energy-consuming industrial loads with green power. However, an inadequate power supply configuration may lead to economic and reliability issues. To address this problem, effective capacity allocation within the green power alternative isolated network is proposed. The capacity allocation process starts with the design of a network structure that aligns with local conditions. Subsequently, a capacity allocation model is developed, considering economic factors, renewable energy utilization efficiency, and system reliability. The gray wolf optimizer is enhanced to establish a capacity allocation method for the green power alternative isolated network. This method is then employed to simulate and assess the performance of the network. The results indicate that the green alternative isolated grid can successfully facilitate green power substitution, satisfying the energy requirements of the loads.

Keywords: green power substitution; capacity allocation; electrolytic aluminum; improvement of gray wolf optimizer



Citation: You, M.; Wang, Y.; Wang, H.; Wusiman, A.; Lv, L. Research on Capacity Configuration for Green Power Substitution in an Isolated Grid Containing Electrolytic Aluminum. *Energies* **2024**, *17*, 2136. <https://doi.org/10.3390/en17092136>

Academic Editor: Dino Musmarra

Received: 3 April 2024

Revised: 26 April 2024

Accepted: 27 April 2024

Published: 30 April 2024



Copyright: © 2024 by the authors. Licensee MDPI, Basel, Switzerland. This article is an open access article distributed under the terms and conditions of the Creative Commons Attribution (CC BY) license (<https://creativecommons.org/licenses/by/4.0/>).

1. Introduction

To address the energy crisis and mitigate the impact of global warming on human society, energy conservation, emissions reduction, and the development of a low-carbon economy have become the prevailing trends in the energy sector worldwide. In recent years, the expansion of China’s wind and photovoltaic power generation capacity connected to the grid has led to increasingly severe energy consumption challenges. The phenomenon of wind and solar energy waste not only squanders investments in clean energy and resources but also, to some extent, hampers the development of subsequent wind and photovoltaic power initiatives. High-energy-consuming loads are characterized by their large unit capacities and concentration. According to data from 2015, mentioned in the literature [1], the power consumption per ton for electrolytic aluminum production was 13,000–14,000 kWh, for electrolytic manganese production it was 5400–6200 kWh, and for iron and steel production, it was 450–500 kWh. Among these, electrolytic aluminum had the highest total power consumption, exceeding that of iron and steel and being significantly higher than other high-energy-consuming loads. Electrolytic aluminum is noted for both its high unit energy consumption and high total energy consumption. By 2021, the shares of thermal power and hydropower in China’s aluminum consumption were 82% and 16%, respectively, while other renewable energy sources remained relatively marginal, indicating an urgent need for green transformation in the aluminum industry.

Usually, self-owned power plants for aluminum electrolysis are generally constructed near hydroelectric stations, but with technological advancements, this situation is likely to change significantly in the future. Firstly, the technologies for wind power and photovoltaic power are rapidly advancing. The cost of wind power has already become lower than that

of thermal power, and the cost of photovoltaic power is also lower than that of most thermal power. The costs of photovoltaic and wind power are approaching those of hydroelectric power, and in the future, they are expected to be lower than hydroelectric costs. Secondly, the locations where China's rivers can accommodate hydroelectric construction are nearly saturated, and hydroelectric power is easily affected by seasonal variations, thus impacting aluminum electrolysis production. Lastly, among the top three provinces in China in terms of aluminum electrolysis capacity are Xinjiang and Inner Mongolia, which cannot provide large amounts of hydroelectric power for aluminum electrolysis loads. However, these regions have abundant wind and solar resources. Therefore, utilizing renewable energy to replace high-energy-consuming loads in such areas is a suitable choice. Hence, green energy alternatives for aluminum electrolysis should consider making appropriate plans based on corresponding scenarios.

In areas abundant in wind and solar energy, constructing an isolated network for green power replacement of high-energy-consuming loads, exemplified by aluminum electrolysis [2], is extremely meaningful. It is important to study the construction of isolation networks for green power substitution of high energy-consuming loads, which is an effective strategy to ensure the local consumption of renewable energy, optimize the utilization of these resources, and advance the replacement of green power in energy-intensive industries.

Numerous studies have been conducted on the capacity allocation of green power alternatives. Literature [3] evaluates the potential for green power substitution in rail transportation. Literature [4] proposes three models of charging stations: one with an energy storage system, one with a photovoltaic system, and one combining both systems. It was demonstrated that the combined photovoltaic and energy storage system could reduce costs while promoting the use of green electricity. Literature [5] establishes a multi-objective optimal allocation model for charging stations, aiming to minimize the annual construction cost, the cost of abandoned light and lost load, and the total emission cost annually. Literature [6] develops a design model for highway microgrids using wind and solar resources, focused on minimizing the annualized integrated cost for microgrid capacity allocation. Literature [7] discusses a microgrid with a school as the case study, optimizing the power supply configuration with economic considerations. Literature [8] examines a direct-supply system in buildings, focusing on improving the load supply rate and smoothing the power consumption curve with two optimization objectives, and explores equipment capacity configuration methods for the building's Power-Energy-Demand Flexibility (PEDF) system. Literature [9] focuses on an independent microgrid in a plateau area, proposing an optimization method for configuring power supply capacity based on typical meteorological years and time-shifted oxygen production loads. The goal is to minimize the average annual cost over the microgrid's lifecycle. Literature [10] optimizes the power capacity allocation for an integrated wind, solar, hydrogen, and storage power supply system, establishing a model to minimize unit power generation costs. Literature [11] formulates a mathematical model for each unit in a grid-connected microgrid, proposing an operational strategy and a comprehensive capacity optimization objective function considering average annual investment costs, operation and maintenance costs, replacement costs, outage compensation, power purchase costs, operational revenue, and end-of-life recycling benefits. Literature [12] proposes a wind-solar-hydrogen microgrid capacity allocation method based on cooperative games, considering the uncertainties of wind and solar energy, and aims to maximize the monthly net return on invested capacity. Literature [13] proposes an optimization model for storage capacity allocation from the power plant side, prioritizing the reduction of average photovoltaic power volatility and storage system costs with a two-tiered optimization approach focusing on both cost and volatility minimization.

Literature [14] constructs an optimal energy storage capacity allocation model aimed at achieving the best capacity ratio and minimizing investment costs. It introduces a discrete particle swarm algorithm to solve the model and obtain the optimal energy storage capacity

allocation results. Literature [15] develops a two-layer optimization model for energy systems in rural areas, employing a particle swarm algorithm combined with mixed integer linear programming to determine the optimal configuration. Literature [16] is based on a composite energy system optimal planning and configuration method, along with a hybrid optimization algorithm proposed in this study. It focuses on comprehensive optimization objectives, including whole life cycle cost (LCC) and minimal energy consumption, for optimal capacity allocation. The study analyzes the results of energy system capacity allocation under various optimization objectives and operational performance on a typical day. Literature [17] establishes a two-layer collaborative optimization model that addresses both system capacity planning and dispatch operations. The upper layer optimizes capacity allocation with goals of efficiency and economy, while the lower layer focuses on minimizing operating costs to achieve the best solution. Literature [18] constructs an optimization objective function that emphasizes comprehensive performance, supplemented by investment costs. It proposes a two-stage capacity optimization allocation method based on orthogonal design preferences and intelligent algorithm optimization. Literature [19] rationalizes the allocation of each power source in residential areas with the objective of maximizing annual benefits. Literature [20] delineates a tripartite capacity with the goal of maximizing each investor's return while considering operating costs. Literature [21] targets the average annual return over the operating life of wind, solar, and storage equipment as the optimization objective and adopts three game models for the rational allocation of these resources. Literature [22] proposes a method to calculate the equipment capacity of a hybrid PV–wind–battery system, as well as to balance generation and demand power, aiming to minimize annual energy production costs and solve the capacity allocation issue. Literature [23] prioritizes economy, introduces a lost-load penalty function, as well as a power-abandonment penalty function, and seeks to minimize comprehensive costs and expenses as the objective function to derive the optimal configuration of wind, solar, diesel, and storage systems.

Literature [24,25] considers the reliability and economy of microgrids to find the optimal solution for microgrid power supply. Literature [26] evaluates the reliability of power supply, the complementary characteristics of wind and solar power, and power fluctuations in the grid from both independent and grid-connected operations, with the goal of minimizing system costs as the objective for capacity allocation. The results of the above studies on green power substitution show that the penetration rate of green power can be significantly increased through rational allocation. However, these studies primarily focus on green power substitution systems for transportation and parks, revealing some limitations in the capacity allocation for industrial loads. In exploring capacity allocation for green power alternative systems for industrial loads, Literature [27] establishes a multi-objective optimal allocation model aimed at maximizing the annual net return of the microgrid, with a particular focus on maximizing in situ PV consumption rate. Literature [28,29] constructs a multi-objective optimization model for the optimal allocation of energy storage capacity in industrial PV microgrids, with the objectives of maximizing PV utilization and annual net profit. Literature [30] optimizes wind and solar capacity in the captive power plant of aluminum electrolysis enterprises with an economic focus, but it does not consider the flexibility transformation of thermal power units, which limits the study's potential to enhance the green power penetration rate in aluminum electrolysis.

To address a series of issues caused by irrational allocation and to provide a reliable reference scheme for promoting green power substitution in high energy-consuming loads, we have chosen Xinjiang, China, as the case study. Here, we design a topology for green power substitution specifically tailored for aluminum electrolysis, combining the local actual conditions. We also propose a capacity allocation solution method based on the improved gray wolf optimizer, which effectively resolves the capacity allocation model. This method allows us to compare different configuration schemes and select the optimal one.

2. Topology and Operation Strategy of Green Power Substitution Isolated Grids

Wind power generation is subject to instability and uncontrollability. The output from a wind farm with an installed capacity of 200 MW over ten days is depicted in Figure 1. Similarly, photovoltaic power generation also experiences these issues. Consequently, when connecting high-energy-consuming loads to renewable energy sources, it is essential to have an adequate number of flexible power sources to mitigate the uncertainty inherent in renewable energy generation.

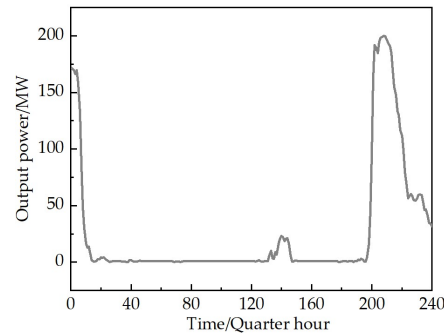


Figure 1. A 200 MW wind farm is part of the historical contribution.

2.1. Topology of Green Power Substitution Isolated Grids

The “Three North” region of China is abundant in coal resources, which makes the construction of thermal power units less geographically restrictive. Opting for thermal power units that have been modified for flexibility as the flexible power sources in green energy alternatives for isolated grids capitalizes on the region’s vast coal resources. This approach addresses the variability of renewable power generation and ensures the stable operation of the system.

Thus, the green power alternative isolated grid system comprises renewable energy sources, such as wind and photovoltaic power, along with energy storage and thermal power units that have been enhanced for flexibility. This paper will analyze three scenarios for capacity allocation within the green power alternative isolated grid system. Scenario 3 is illustrated in Figure 2, while the other two scenarios share similarities with Figure 2.

Scenario 1: photovoltaic power + flexibility modified thermal unit;

Scenario 2: wind power + flexibility modified thermal unit;

Scenario 3: wind power + photovoltaic power + flexibility modified thermal unit.

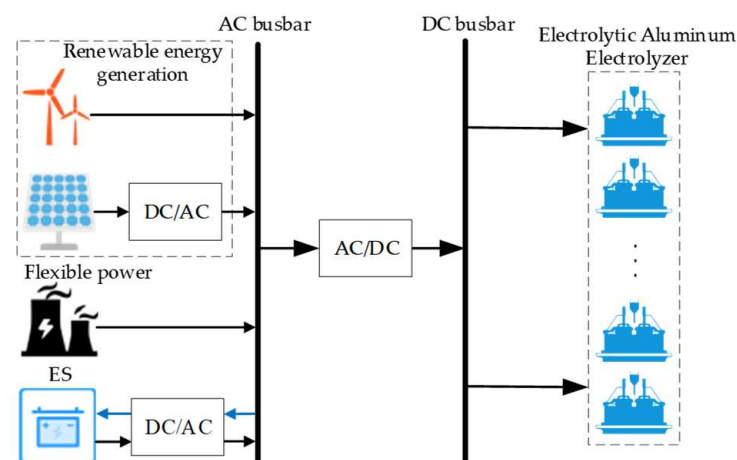


Figure 2. Topology of green power substitution isolated grids.

2.1.1. Wind Power Model

The relationship between wind speed and the wind turbine’s power output can be approximated by Equation (1).

$$WT(t) = \begin{cases} 0 & 0 \leq v < v_{ci} / v \geq v_{co} \\ \frac{P_r(v-v_{ci})}{v_r-v_{ci}} & v_{ci} \leq v \leq v_r \\ P_r & v_r \leq v < v_{co} \end{cases} \quad (1)$$

where v_{ci} is the tangential wind speed at the wind turbine; v_r is the rated wind speed; v_{co} is the tangential wind speed; P_r is the rated output power of the wind turbine. When the wind speed is between v_{ci} and v_r , the wind turbine’s output power is approximately linear.

2.1.2. Photovoltaic Power Generation Model

The output of photovoltaic power generation is primarily influenced by factors such as solar radiation and ambient temperature. The relationship between its output and these factors is expressed in Equation (2).

$$PV(t) = P_{stc} \frac{E_a}{E_{stc}} [1 + \downarrow(t_a - t_{stc})] \quad (2)$$

where E_{stc} represents the standard conditions of solar irradiance, E_a is the workplace solar irradiance at the workplace, t_{stc} denotes the standard conditions of temperature, t_a is the workplace temperature, \downarrow is the power temperature coefficient, P_{stc} represents the standard conditions of the solar power generation system’s rated power, $PV(t)$ represents the output power of the photovoltaic power generation system at the operating point at time t .

2.1.3. Energy Storage Model

The state of charge (SOC) of the energy storage device at time $t + 1$ is determined by the electricity supply and demand in the system at the previous moment, time t , as shown in Equation (3).

$$S_{ee}(t + 1) = \begin{cases} S_{ee}(t) + \frac{P_{cha}(t)\Delta t}{\eta_{cha}} \\ S_{ee}(t) - \eta_{dis}P_{dis}(t)\Delta t \end{cases} \quad (3)$$

where $S_{ee}(t)$ and $S_{ee}(t + 1)$ denote the charge capacity of the energy storage system at times t and $t + 1$, respectively; $P_{cha}(t)$ and $P_{dis}(t)$ represent the charging power or discharge power of the energy storage system at time t , respectively; η_{cha} and η_{dis} are the charging and discharging efficiencies of the energy storage system, respectively.

2.1.4. Peak Shaving Cost Model of Thermal Power Units

The operational process of thermal power units can be categorized based on regulation capacity and cost characteristics into regular peak regulation (RPR) and deep peak regulation (DPR), with the latter subdivided into oil-free deep peak regulation (DPR) and oil-assisted deep peak regulation (ODPR), depending on whether oil is used during operation. The peak shaving process is depicted in Figure 3.

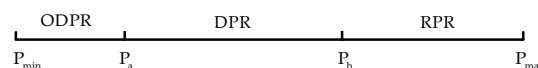


Figure 3. Schematic diagram of the peak regulation process of thermal power units.

During the regular peaking phase (RPR), the peaking cost consists of fuel expenses, typically calculated using the coal consumption characteristic function, as shown in Equation (4).

$$C_{coal}(P_{th}(t)) = (aP_{th}(t)^2 + bP_{th}(t) + c)q_{coal} \quad (4)$$

where P_{th} is the unit output power; a, b, c are coefficients of the quadratic, linear, and constant terms of the unit consumption characteristic function, respectively, and their values depend on the type of thermal power unit, the boiler type, and the coal quality; q_{coal} represents the coal price.

During deep peaking operations (DPR), thermal power units operate away from their design values, significantly decreasing power generation efficiency, shortening unit lifespan, and increasing generation costs. The loss cost of the unit can be estimated using the Manson–Coffin formula, which considers the number of cycles in the fracturing cycle, as shown in Equation (5).

$$C_{life}(P_{th}(t)) = \frac{1}{N_t} C_{th} \tag{5}$$

In oil-free deep peaking (ODPR), the unit’s cost is the sum of the fuel cost and the unit’s loss cost. During deep peaking with oil, the unit requires oil injection to maintain normal operation, thus necessitating the inclusion of oil injection costs at this stage. Overall, thermal power units exhibit different characteristics during various peaking stages, and their peaking costs are presented in Equation (6).

$$C_{th,p}(t) = \begin{cases} C_{coal}(P_{th}(t)) & P_b \leq P_{th}(t) \leq P_{max} \\ C_{coal}(P_{th}(t)) + C_{life}(P_{th}(t)) & P_a \leq P_{th}(t) \leq P_b \\ C_{coal}(P_{th}(t)) + C_{life}(P_{th}(t)) + C_{oil}(P_{th}(t)) & P_{min} \leq P_{th}(t) \leq P_a \end{cases} \tag{6}$$

2.1.5. Controllable Load Characteristics of Electrolytic Aluminum

The electrolytic aluminum load is a typical heat storage type load with significant thermal inertia. The normal operating temperature for aluminum electrolysis loads is between 950 and 970 degrees Celsius. High temperature requirements exist during the operation of aluminum electrolysis loads, necessitating continuous energy supply to maintain stable operations.

Figure 4 shows the equivalent circuit model of aluminum electrolysis [31]. In this model, V_{AH} and V_{AL} represent the high- and low-voltage side voltages of the AC busbars, respectively; k denotes the turns ratio of the on-load tap changer, and L_{SR} stands for the equivalent inductance value of the saturable reactor. V_d and I_d represent the DC voltage and DC current of the electrolytic cell, respectively. E_d and R_d represent the counter electromotive force and equivalent resistance inside the electrolytic cell. As indicated in Figure 4, the active power of the electrolytic aluminum load can be effectively controlled by adjusting the AC side voltage, the on-load transformer ratio, and the saturation reactor voltage.

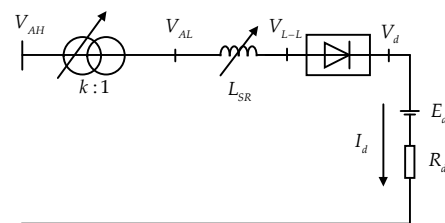


Figure 4. The equivalent circuit model of aluminum electrolysis.

The power of the electrolytic aluminum load is shown in Equation (7).

$$P_{ASL} = V_d I_d = \frac{V_d(V_d - E_d)}{R_d} \tag{7}$$

The quantitative relationship between the DC voltage V_d and the high-voltage side bus voltage V_{AH} is illustrated in Equation (8) [32].

$$V_d = \left(\frac{1.35V_{AH}}{k} + \frac{3\omega L_{SR}}{2\pi R_d} E_d \right) / \left(1 + \frac{3\omega L_{SR}}{2\pi R_d} \right) \quad (8)$$

Here, ω represents the angular frequency of the system. Given that the frequency of the system changes minimally during the frequency process, its variation is neglected in Equation (8). During the control process, the saturated reactor exits steady current control, and the inductance of the saturated reactor is assumed to be constant. After applying linearization using the Taylor expansion method, Equation (9) is derived from the linearized Equation (8).

$$\Delta V_d = \frac{2.7\pi R_d}{2k\pi R_d + 3\omega L_{SR}} \Delta V_{AH} = K_{L2} \Delta V_{AH} \quad (9)$$

Substituting Equation (9) into Equation (7) yields the corresponding relationship between the voltage change at the generator terminal and the change in active power of the load, as shown in Equation (10).

$$\Delta P_{ASL} = a^2 \Delta V_{AH}^2 + b \Delta V_{AH} \quad (10)$$

The relationship between the change in voltage at the generator end and the change in active power of the load is established through Equation (10). According to Equation (10) and corroborated by field tests referenced in [33], the power of the electrolytic aluminum load can quickly respond to the regulation signal, with a regulation capability of up to 15% of the rated power.

2.2. Operation Strategy

To satisfy the energy requirements of aluminum electrolysis and maximize the consumption of green power, a systematic operational strategy must be devised. The strategy should adhere to the principle: “reduce thermal power output first when there is excess new energy generation, followed by charging the energy storage, and when new energy generation is insufficient, discharge the energy storage first, followed by increasing thermal power output”.

- (1) When $t = 1$, when the sum of new energy generation and thermal power output is considered, if it exceeds aluminum demand at minimum thermal power output, energy storage systems should charge. If the storage cannot absorb the surplus power, the system must discard it. Conversely, if the combined output of new energy generation and thermal power is less than the aluminum demand, the strategy should prioritize discharging from storage and increasing the thermal power output. If these measures cannot meet the demand, it is assumed that the load of the electrolytic aluminum will be correspondingly reduced.
- (2) If the sum of new energy and the thermal power output from the previous moment exceeds the demand for electrolytic aluminum and the state of charge of the energy storage is below maximum, the thermal power unit should reduce its output, and the energy storage should be charged. If neither can absorb the excess, the system discards the surplus power to achieve equilibrium. If the energy storage charge level is at or above the maximum, the thermal power output should be reduced to absorb the excess energy, discarding any surplus to maintain balance. On the other hand, if the output from new energy and thermal power units from the previous moment is less than the electrolytic aluminum demand and the energy storage charge level is above the minimum, the storage should discharge, and thermal power should increase its output to reach equilibrium. If the charge level is at or below the minimum, thermal power should increase its output to achieve balance. If it is not possible to meet the

shortfall, it is assumed that the electrolytic aluminum load will decrease accordingly to maintain system power balance.

3. Alternative Grid Capacity Allocation Model for Green Electricity

3.1. Industrial Grid System Model

The aim of allocating capacity for electrolytic aluminum in isolated grids using green power alternatives is to balance the utilization rate of green energy with the reliability of the system's energy supply. This is achieved by judiciously allocating capacities among wind turbines, PV modules, energy storage systems, and thermal power units, while also considering the system's economy. The objective function for the green power alternative isolated grid with electrolytic aluminum is presented in Equation (11).

$$\min F = (f_1, f_2, f_3)_{\min} \quad (11)$$

where f_1 is the total cost of the system; f_2 is the curtailment rate of the system; f_3 is the power shortage rate of the system.

3.1.1. Total System Cost

The total cost of the green power alternative isolated grid encompasses the investment cost for power supply, C_a ; the cost of thermal unit peaking, $C_{th,p}$; operation and maintenance expenses, C_{om} ; and the environmental costs associated with tail gas emissions, C_t . These components are detailed in Equation (12).

$$f_1 = C_a + C_{th,p} + C_{om} + C_t \quad (12)$$

The average annual initial investment cost for each power source within the isolated grid is expressed in Equation (13) [34].

$$C_a = \sum_{i=1}^n (N_i C_{s,i} \frac{\gamma(1+\gamma)^{y_i}}{(1+\gamma)^{y_i} - 1}) \quad (13)$$

where n is the number of power supply types; N_i is the number of power supplies of type i ; $C_{s,i}$ is the unit cost of the power supply type i ; γ is the discount rate; and y_i is the service life of the power supply type i .

The annual O&M cost of the lone network is shown in Equation (14).

$$C_{om} = \sum_{i=1}^n c_{om,i} N_i \quad (14)$$

where $c_{om,i}$ is the unit O&M cost of Type i power supply.

The cost of an isolated network environment is shown in Equation (15).

$$C_t = \sum_i^m p_i q_i \quad (15)$$

where p_i is the i -type exhaust emission factor; q_i is the i -type exhaust gas treatment cost.

3.1.2. System Curtailment Rate

When the system generates excess power that cannot be consumed, power curtailment is necessary to maintain the system's power balance. The curtailment rate is defined in Equation (16).

$$f_2 = \frac{\sum_{t=1}^T (PV(t)\Delta t + WT(t)\Delta t - PV'(t)\Delta t - WT'(t)\Delta t)}{\sum_{t=1}^T (PV(t)\Delta t + WT(t)\Delta t)} \tag{16}$$

where $PV(t)$ and $WT(t)$ are the photovoltaic output and wind power output that can be theoretically obtained according to the time t wind and solar data, and $PV'(t)$ and $WT'(t)$ are the actual PV and wind power output.

3.1.3. System Power Supply Reliability

To ensure the normal operation of the electrolytic aluminum load within the system, the load shortage rate is used to assess the reliability of the system’s power supply. A lower load-shortage rate indicates greater reliability. If the system is unable to meet the load demand, it is necessary to curtail the corresponding load to achieve power balance. The formula for the power shortage rate is shown in Equation (17).

$$f_3 = \frac{\sum_{t=1}^T P_{bre}(t)\Delta t}{\sum_{t=1}^T P_{load}(t)\Delta t} \tag{17}$$

where $P_{bre}(t)$ is the power deficit when the system cannot meet the load demand; $P_{load}(t)$ is the load power of electrolytic aluminum.

3.2. Capacity Configuration Constraints

The power generated by renewable energy sources in the isolated grid system at any given time must satisfy a value less than or equal to the theoretical value. The operation of thermal units should meet the power constraints. The power for storage charging and discharging, along with the state constraints of nuclear power, must comply with reasonable limits. The above constraints are shown in Equation (18). Additionally, the number of power sources should conform to Equation (19).

$$\left\{ \begin{array}{l} 0 \leq WT'(t) + PV'(t) \leq WT(t) + PV(t) \\ P_{th,min} \leq P_{th}(t) \leq P_{th,max} \\ -\Delta P_{th}^{down} \Delta t \leq P_{th}(t+1) - P_{th}(t) \leq \Delta P_{th}^{up} \Delta t \\ SOC_{min} < SOC(t) < SOC_{max} \\ 0 \leq P_{cha}(t) \leq P_{cha,max} \\ 0 \leq P_{dis}(t) \leq P_{dis,max} \end{array} \right. \tag{18}$$

$$\left\{ \begin{array}{l} 0 \leq N_1 \leq N_{1,max} \\ 0 \leq N_2 \leq N_{2,max} \\ 0 \leq N_3 \leq N_{3,max} \\ 0 \leq N_4 \leq N_{4,max} \end{array} \right. \tag{19}$$

where $N_1, N_{1,max}$ represent, respectively, the number of wind turbine configurations and the maximum number of installations; $N_2, N_{2,max}$ represent, respectively, the number of photovoltaic module configurations and the maximum number of installations; $N_3, N_{3,max}$ represent, respectively, the number of thermal power generator configurations and the maximum number of installations; $N_4, N_{4,max}$ represent, respectively, the number of energy storage module configurations and the maximum number of installations.

4. Improvement of the Gray Wolf Algorithm and Solution Flow

4.1. Gray Wolf Colonies and Their Predatory Behavior

The GWO algorithm is a swarm intelligence optimization technique developed by Mirjalili et al. [35], scholars from Griffith University, Australia, in 2014. Inspired by the prey hunting behavior of gray wolves, this algorithm exhibits strong convergence performance, has few parameters, and is easy to implement.

Gray wolves are members of the canine family and typically live in groups, averaging 5–12 individuals per pack. A strict hierarchy exists within a gray wolf pack, as depicted in Figure 5.

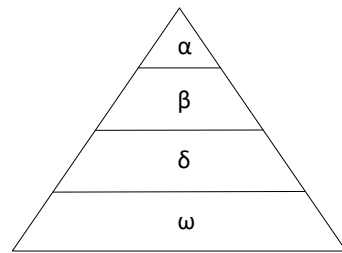


Figure 5. Gray wolf population hierarchy map.

The leader, or α , of the pack has the responsibility of managing the group and is at the top of the hierarchical pyramid, in charge of activities such as hunting, habitat selection, and food distribution. Immediately below the α is the β , who assists the α and is second in the pack’s dominance hierarchy. The δ wolves occupy the third level of the pyramid, taking directions from both the α and β . At the bottom of the pyramid are the ω wolves, whose primary role is to maintain the pack’s numbers. The hierarchy within the pack is dynamic; older wolves may be demoted if their performance diminishes, while younger wolves may be promoted if they excel. The predation behavior of gray wolves typically involves the following steps:

- (1) Searching for, tracking, and approaching the prey;
- (2) Encircling the prey;
- (3) Attacking the prey.

4.2. Gray Wolf Optimizer Model

The gray wolf optimizer emulates the social hierarchy and hunting tactics of gray wolves in nature. The entire wolf pack is categorized into four distinct levels. The top three levels, consisting of the most adaptable groups, lead the rest of the wolves, denoted as ω , in the hunt for prey. During the search, ω wolves orbit around the leading three groups to update their positions.

$$\begin{cases} D_\alpha = |C_1 X_\alpha(t) - X| \\ D_\beta = |C_2 X_\beta(t) - X| \\ D_\delta = |C_3 X_\delta(t) - X| \end{cases} \quad (20)$$

$$\begin{cases} X_1 = X_\alpha - A_1 D_\alpha \\ X_2 = X_\beta - A_2 D_\beta \\ X_3 = X_\delta - A_3 D_\delta \end{cases} \quad (21)$$

$$A = 2ar_1 - a \quad (22)$$

$$C = 2r_2 \quad (23)$$

In Equation (20), D_α , D_β , and D_δ denote the distance between α , β , and δ from other individuals, respectively; X_α , X_β , and X_δ represent the current positions of α , β , and δ , respectively; C_1 , C_2 , and C_3 are random vectors, and X is the position of the current gray wolf. Equation (21) defines the step size and direction of the wolves in pack ω towards

the other three groups of wolves, respectively. Equations (22) and (23) are the calculation methods for A and C , respectively, where α is the convergence factor, which decreases linearly from 2 to 0 with the number of iterations, and r_1 and r_2 are the random numbers between the modulo $[0,1]$.

In this section, the gray wolf optimizer’s mathematical model is presented. It is worth noting that the model does not guarantee finding the global optimum; instead, during the iterative process, there is a tendency to converge on local optima as it moves towards the other three wolf groups.

4.3. Improved Gray Wolf Optimizer

- (1) A dynamic weighting strategy is introduced to expedite the convergence of the gray wolf optimizer. Proportional weighting based on step Euclidean distance has proven to be effective. Therefore, this paper implements a proportional weighting approach premised on step Euclidean distance [36].
- (2) Nonlinearization of the convergence factor. To prevent the gray wolf optimizer from succumbing to local optima, the parameter σ_1^2 is adjusted to be larger in the initial phase and smaller in the latter phase. This paper introduces a convergence factor modeled after the normal distribution density function’s decay pattern. By altering the value of σ_2^2 , the decay rate of the normal distribution density function can be modified. The improved convergence factor is expressed in Equation (24).

$$a = \begin{cases} a_{initial} e^{-\left(\frac{l}{l_{max}}\right)^2 / (2\sigma_1^2)} & l \leq 0.5l_{max} \\ a_{initial} e^{-\left(\frac{0.5l_{max}}{l_{max}}\right)^2 / (2\sigma_1^2)} e^{-\left(\frac{l}{l_{max}} - 0.5\right)^2 / (2\sigma_2^2)} & 0.5l_{max} \leq l \leq l_{max} \end{cases} \quad (24)$$

where $a_{initial}$ is the initial value of a of the convergence factor (in this paper, the initial value of a is taken to be 2), l is the current number of iterations, l_{max} is the maximum number of iterations, while σ_1^2 and σ_2^2 are the convergence factor adjustment parameters.

When σ_1^2 is set to 0.08, σ_2^2 is set to 0.0064, as indicated in Figure 6, the value of a regulation of the improved gray wolf algorithm decays slowly in the early stage, which is conducive to the global exploration capability of the algorithm, and decays quickly in the later stage, which can effectively improve the convergence of the algorithm.

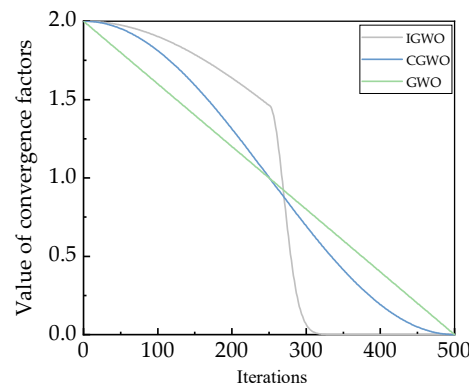


Figure 6. The comparison of convergence factors.

To more intuitively reflect the advantages of the improved gray wolf optimizer, four test functions were selected, and both the original gray wolf optimizer and the improved gray wolf optimizer were used as controls, in which $y_1(x)$ and $y_2(x)$ were single-peak benchmark functions, and $y_3(x)$ and $y_4(x)$ were multi-peak benchmark functions. The test

results are shown in Figure 7. It should be noted that the $y_4(x)$ searched for an optimal solution 500 times, but the optimal solution was found in fewer than 200 attempts.

$$\left\{ \begin{array}{l} y_1(x) = \sum_{i=1}^n x_i^2 \\ y_2(x) = \sum_{i=1}^n |x_i| + \prod_{i=1}^n |x_i| \\ y_3(x) = -20 \exp\left(-0.2 \sqrt{\frac{1}{n} \sum_{i=1}^n x_i^2}\right) - \exp\left(\sqrt{\frac{1}{n} \sum_{i=1}^n \cos(2\pi x_i)}\right) + 20 + \exp(1) \\ y_4(x) = \frac{1}{4000} \sum_{i=1}^n x_i^2 - \prod_{i=1}^n \cos\left(\frac{x_i}{\sqrt{i}}\right) + 1 \end{array} \right. \quad (25)$$

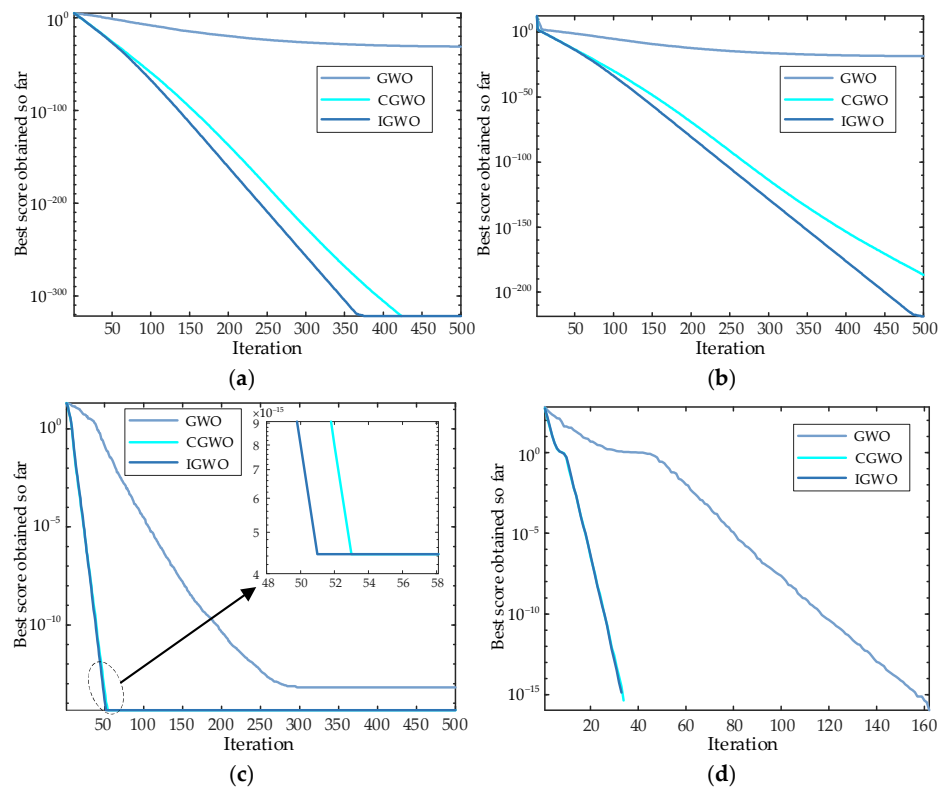


Figure 7. Graphs of the results of the four test functions. (a) Convergence plot of $y_1(x)$; (b) convergence plot of $y_2(x)$; (c) convergence plot of $y_3(x)$; (d) convergence plot of $y_4(x)$.

Figure 6 shows the solution process of the four test functions using the original gray wolf algorithm, the improved gray wolf optimizer, and the CGWO proposed in this paper for the optimal solution of the test functions. It can be seen that in the single-peak function solving process, the improved gray wolf algorithm proposed in this paper is significantly better than the original gray wolf algorithm and the CGWO; in the multi-peak test function solving process, the improved gray wolf algorithm proposed in this paper is significantly better than the original gray wolf algorithm, and the CGWO is not much different from the results. In conclusion, the improved gray wolf algorithm proposed in this paper has good results.

4.4. A Configuration Solution Method Based on the Improved Gray Wolf Optimizer

According to the energy operation strategy, combined with the improved gray wolf optimizer, the solution steps are as follows (the solution flowchart is shown in Figure A1 of Appendix A):

- (1) Enter the data of wind speed, light intensity, temperature and load data for 8760 h of the year;

- (2) Set the parameters of the power supply, initialize the wolf pack size N , the maximum number of iterations l_{\max} , the value in the convergence factor, and the upper and lower limits of the optimization variables to generate the initial wolf pack;
- (3) Based on the wind and solar data, the output of a single wind turbine and photovoltaic is obtained. The objective function value is solved based on the scheduling strategy and relevant parameters, and it is used as the fitness of the gray wolf. The top three fitness values are denoted as wolves α, β, δ , and their positions are denoted as X_α, X_β , and X_δ ;
- (4) When $l \geq l_{\max}$, the optimal value is output, and when the solution is completed, if $l < l_{\max}$, then step (3) is executed;
- (5) According to Equation (25), the nonlinear convergence factor α is updated, A and C are updated according to Equations (22) and (23), the position of the gray wolf is updated according to Equation (21), the individual fitness is recalculated until the termination condition is satisfied, and the optimal capacity configuration result is output.

5. Parameter and Result Analysis

5.1. Parameters

Figure 8 shows the hourly weather data for a place in Xinjiang. Initialize the wolf pack size $N = 1000$ and the maximum number of iterations as $l_{\max} = 100$. The electrolytic aluminum load is 680 MW, and since the green power system mentioned in this article serves electrolytic aluminum, it is assumed that the electrolytic aluminum operates at maximum power throughout the year. The remaining parameters are shown in Table A1 of Appendix A.

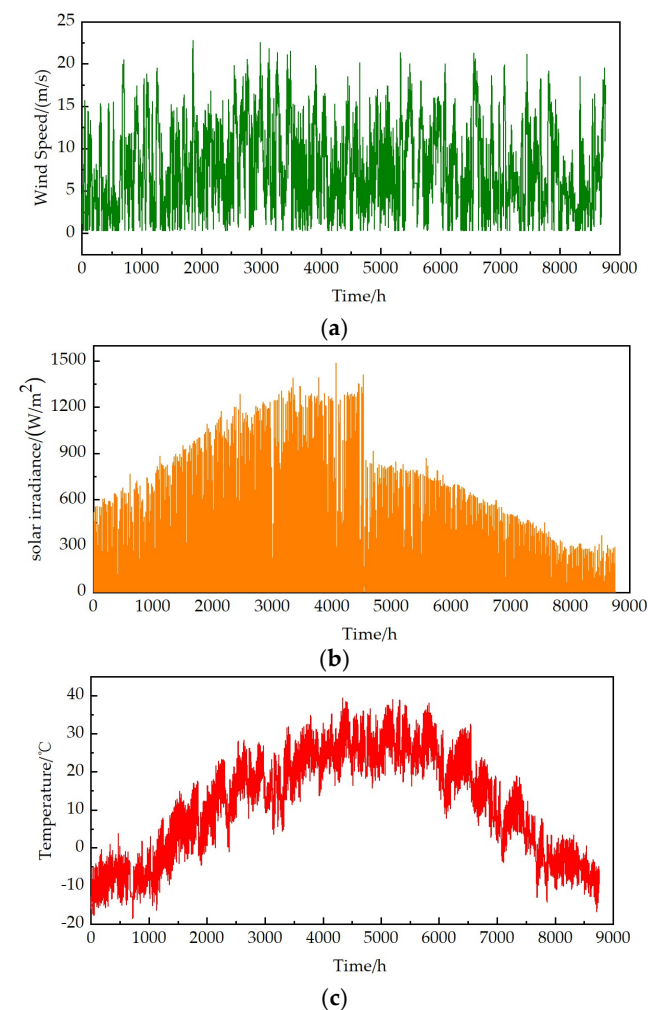


Figure 8. Hourly weather data throughout the year. (a) Hourly wind speed throughout the year. (b) Hourly solar irradiance throughout the year. (c) Hourly temperature throughout the year.

5.2. Analysis of Results

(1) Analysis of the economics of total investment

As indicated in Table 1 and Appendix A of Table A1, among the scenarios, Scenario 3 has the highest installed capacity for renewable energy generation, at 580.741 MW, with Scenario 2 at 504 MW, and Scenario 1 at 471.567 MW. As depicted in Table 2, the total cost for Scenario 2 is the lowest, at CNY 1667.29702 M which is less than the total costs of CNY 1734.61290 M for Scenario 3 and CNY 1830.30371 M for Scenario 1, representing a reduction of 8.906 percent from Scenario 1 and 3.881 percent from Scenario 3. The total cost for Scenario 3 is 5.228 percent lower than that of Scenario 1.

Table 1. The configuration result in three scenarios.

Scenarios	Number of Wind Turbines	Number of PV Modules	Number of Thermal Power Units	Number of Energy Storage Components
1	0	437	2	198
2	168	0	2	199
3	122	199	2	197

Table 2. Result of each objective.

Scenarios	Objective Function f_1 /CNY	Objective Function f_2 /%	Objective Function f_3 /%
1	1830.30371 M	0.541	6.647
2	1667.29702 M	0.220	2.826
3	1734.61290 M	0.701	1.970

From an economics standpoint of total investment, Scenario 2 is the most favorable, followed by Scenario 3, and lastly, Scenario 1, when considering only economics of total investment factors. Table A2 in Appendix B details the unit cost, operating cost, cost related to thermal peaking, and environmental costs for the three scenarios.

(2) Renewable energy utilization analysis

Figure A2 in Appendix C presents the hourly generation and curtailment throughout the year. In order to conveniently reflect the utilization rate of green electricity, based on the hourly generation and curtailment for the entire year, the proportion of curtailment is analyzed weekly to obtain the curtailment for all 52 weeks of the year, as shown in Figure 9. As indicated in Figure 9, In Scenario 1, there are more weeks with curtailed electricity compared to the other two scenarios. However, the curtailment rates in Scenario 2 are not high, with the highest not exceeding 0.01. In both Scenario 1 and Scenario 2, the weeks with curtailed electricity are fewer, mainly concentrated between the 15th and 27th weeks, with weekly curtailment rates exceeding 0.03, significantly higher than the highest curtailment rate in Scenario 2.

As shown in Table 3, Figure A2 in Appendix C and Figure 9, among the scenarios, regarding hourly power curtailment, Scenario 3 experiences the most, at 199.467 MW, followed by 154.636 MW in Scenario 1, and the least, at 144.5 MW in Scenario 2. Overall, the average and total power curtailment are greatest in Scenario 3, followed by Scenario 1, and then Scenario 2. Scenario 2 produces the most total green electricity, at 1,871,769.262 MWh, with Scenario 3 generating 1,836,691.928 MWh. The least amount is produced in Scenario 1, at 901,629.849 MWh. The rate of green power substitution for Scenario 1 is significantly lower, at 15.054%, compared to 31.353% for Scenario 2 and 30.617% for Scenario 3.

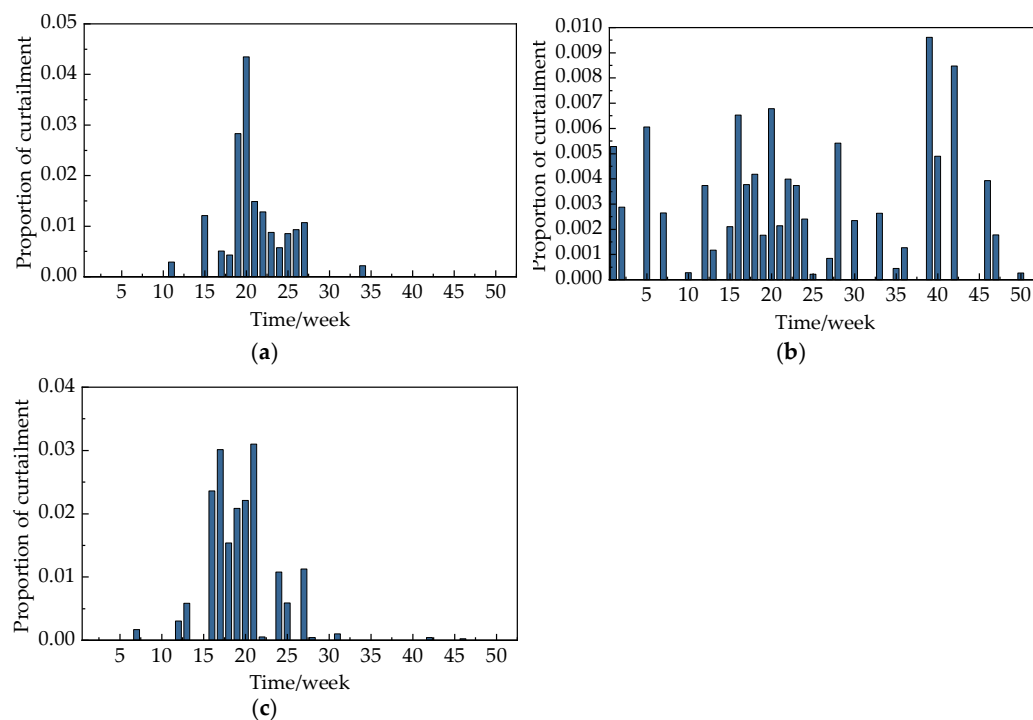


Figure 9. Three scenarios for the annual 52-week proportion of curtailment results. (a) Proportion of curtailment for Scenario 1. (b) Proportion of curtailment for Scenario 2. (c) Proportion of curtailment for Scenario 3.

Table 3. Green electricity production and utilization.

Scenarios	Average Amount of Electricity Curtailed/(MWh)	Total Curtailment/(MWh)	Total Power Generation from Renewable Energy/(MWh)	Green Energy Substitution Rate/%
1	0.558	4884.824	901,629.849	15.054
2	0.471	4126.762	1,871,769.262	31.353
3	1.470	12,881.044	1,836,691.928	30.617

Table A3 in Appendix D shows emission factors and emission benefits. Using the benchmark of 0.123 kg of standard coal consumption per unit of electricity generated, the green electricity in Scenario 1 equates to saving 110,299.638 tons of standard coal, which can reduce emissions by approximately 83,607.126 tons, including a reduction of 80,077.537 tons of CO₂, 2426.592 tons of SO₂, and 1102.996 tons of NO_x, resulting in total environmental benefits worth CNY 21.95967 million. In Scenario 2, the green electricity savings are equivalent to 229,720.028 tons of standard coal, with a reduction in emissions of about 174,127.781 tons, including a CO₂ reduction of 166,776.740 tons, an SO₂ reduction of 5053.841 tons, and an NO_x by 2297.200 tons, generating total environmental benefits of CNY 45.73519 million. For Scenario 3, green electricity consumption corresponds to a saving of 224,328.739 tons of standard coal, reducing emissions by approximately 170,041.184 tons, including reducing CO₂ by 162,862.665 tons, SO₂ by 4935.232 tons, and NO_x by 2243.287 tons, resulting in total environmental benefits of CNY 44.66183 million. The analysis of green power utilization in the three scenarios of the green power alternative isolated grid connecting to electrolytic aluminum demonstrates that incorporating such a high-energy-consuming load can significantly cut down on coal usage, decrease tail gas emissions, and generate substantial environmental benefits.

(3) System power supply reliability analysis

Figure A3 in Appendix C presents the hourly power shortage rate throughout the year, assuming that the electrolytic aluminum load did not participate in regulation. In order to conveniently reflect the power shortage rate, based on the hourly power shortage rate for the entire year, the proportion of curtailment is analyzed weekly to obtain the proportion of load shortage for all 52 weeks of the year, as shown in Figure 10.

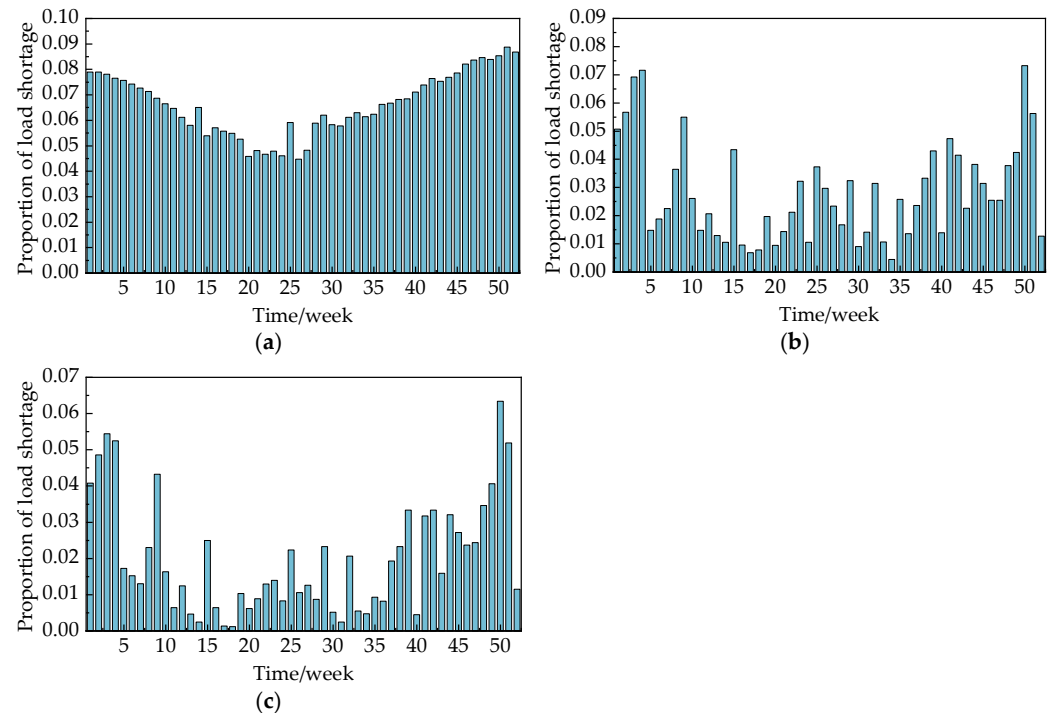


Figure 10. Three scenarios for the annual 52-week proportion of load shortage results. (a) Proportion of load shortage for Scenario 1. (b) Proportion of load shortage for Scenario 2. (c) Proportion of curtailment for Scenario 3.

As shown in Figure 10, Figure A3, and Table 2, Scenario 3 boasts the lowest power shortage rate, at 1.970%, which is better than the 2.826% in Scenario 2 and significantly lower than the 6.647% in Scenario 1. The above weekly data preliminarily suggest the feasibility of all three scenarios. Assuming that the aluminum electrolysis load does not participate in system regulation, all three scenarios experience electricity shortages throughout the year, with Scenario 1 exhibiting the most severe shortages, especially at the beginning and end of the year. The highest shortage rate occurs in the 51st week, exceeding 0.08, while the lowest shortage rate appears in the 26th week. Scenario 2 and Scenario 3 have similar overall shortage rates, both being lower than Scenario 1, with Scenario 3 demonstrating better performance than Scenario 2 in terms of electricity shortages. According to Section 2.1.5, overall, the weekly shortage rates do not exceed 0.1, which is less than 15% of the rated power.

As seen from Figure A3, the maximum power deficit occurs in all three scenarios, at 80 MW. This is because the configuration for all three scenarios consists of two 300 MW thermal power units. Under extremely adverse wind and solar conditions, i.e., when wind and solar power output values are both 0, the system ensures the normal operation of aluminum electrolysis loads by running the two thermal power units at their rated power. The remaining power deficit of 80 MW is managed by reducing the aluminum electrolysis load. Considering the regulation capability of aluminum electrolysis loads to be 15% of the rated power, in this scenario, when the power deficit of the load is less than 102 MW, the aluminum electrolysis loads can operate at reduced power for a period of time. When the power deficit exceeds 102 MW, as shown in Figure A3, the maximum power deficits in

Scenarios 1 and 2 exceed 102 MW, with Scenario 1 and 2 both exceeding 200 MW, while the maximum power deficit in Scenario 3 is approximately 102 MW. Under the consideration of the regulation characteristics of the aluminum electrolysis load, Scenario 3 is more capable of achieving power balance compared to the other two scenarios. Clearly, Scenario 3 is superior to the other two scenarios in terms of reliability.

This analysis considers only one aspect of each scenario. Scenario 2 is the most economically advantageous and also leads in renewable energy utilization. Scenario 3 is slightly less economical, and Scenario 1 is slightly behind in terms of renewable energy utilization compared to Scenario 2. The goal of the green power alternative isolated grid is to fulfill the energy demand of the electrolytic aluminum load as much as possible, using green power and ensuring grid reliability. The total investment cost for Scenario 3 is only CNY 67.31588 M more than that of Scenario 2, which is about a 4.037% increase. This difference in investment costs is relatively minor. Scenario 3's power curtailment rate is 0.856% lower than that of Scenario 1 and is reduced by 30.290% compared to Scenario 2. Although the power curtailment rate of Scenario 3 is 0.481% higher than that of Scenario 2, which is an increase of 218.636%, the power curtailment rates of both Scenarios 2 and 3 are less than 1%. This means that the utilization rate of renewable energy resources is nearly 100%. The slight increase of 0.481% in the power curtailment rate for Scenario 3 has resulted in a lower shortage rate compared to Scenario 2 by 0.856%. Therefore, considering the overall scenario, Scenario 3 is the optimal choice among the three scenarios configured under the historical weather conditions described in the study.

6. Conclusions

This paper evaluates three topological schemes of a green power alternative isolated grid, devises operational strategies based on renewable energy consumption and the load demands of aluminum electrolysis, and establishes a capacity configuration model that considers economy, renewable energy utilization, and reliability. The model is solved using the improved gray wolf optimizer (IGWO), and the results are compared and analyzed, yielding the following conclusions:

- (1) The nonlinearized convergence factor of the GWO has been tested using both single-peak and multi-peak functions. The results show that the GWO proposed in this paper is substantially improved in terms of search capability. This confirms that nonlinearizing the convergence factor achieves a balance between the initial and final phases of the search.
- (2) Utilizing the controllable load characteristics of aluminum electrolysis, when the green power alternative isolated grid cannot entirely satisfy the aluminum electrolysis energy demand, reducing part of the power operation stabilizes and enhances system reliability.
- (3) Within the green power alternative isolated grid, a combination of "multiple renewable energy generation + thermal power unit" proves more stable and reliable than the other two scenarios, albeit at the expense of some economic and renewable energy utilization aspects.
- (4) Through the flexibility of thermal power units, the green power substitution isolated grid can partially replace the energy consumption of aluminum electrolysis with green power while ensuring the normal operation of the electrolysis process.

It should be noted that the research presented in this paper is primarily applicable to new-energy-rich regions with abundant coal resources. These areas can supply large quantities of green power, while coal ensures the regular operation of flexible thermal power units. Large industrial loads serve as a vessel for utilizing substantial amounts of green power. Future studies will consider additional topologies that combine flexible power sources with new energies, along with corresponding capacity allocation models and solution methods.

Author Contributions: Conceptualization, M.Y., Y.W., H.W., A.W. and L.L.; Data curation, M.Y.; Formal analysis, M.Y.; Funding acquisition H.W.; Investigation, M.Y.; Methodology, M.Y.; Project administration H.W.; Resources, M.Y., Y.W., A.W. and L.L.; Software, M.Y.; Supervision H.W.; Validation, M.Y. and H.W.; Visualization, M.Y. and H.W.; Writing—original draft, M.Y.; Writing—review & editing, M.Y. All authors have read and agreed to the published version of the manuscript.

Funding: This research is funded by the Xinjiang Uygur Autonomous Region Key R&D Program Projects (2022B01020-3).

Data Availability Statement: The original contributions presented in the study are included in the article, further inquiries can be directed to the corresponding authors.

Acknowledgments: I am immensely thankful to Haiyun Wang for her patient guidance throughout the development of this paper. I am also deeply appreciative of Haiyun Wang for accepting my participation in this pivotal project and providing me with this invaluable opportunity. Thank you to Yunguang Wang, Aisikaer Wusiman and Liangnian Lv for providing support! Once more, I wish to convey my heartfelt gratitude to my mentor!

Conflicts of Interest: Author Yunguang Wang was employed by the company Goldwind Science & Technology Co., Ltd. The remaining authors declare that the research was conducted in the absence of any commercial or financial relationships that could be construed as a potential conflict of interest.

Appendix A

Table A1. Unit parameter table.

Parameters	Items	Numerical Value/Unit
Wind Power Generation	Stand-alone capacity	3 MW
	The cost of a single machine	CNY 11.34 M
	O&M costs	CNY 376,500/year
	Cut into the wind speed	3 m/s
	Rated wind speed	14 m/s
	Cut out the wind speed service life	25 m/s 20 year
Photovoltaic Power Generation Modules	Stand-alone capacity	1.0791 MW [30]
	The cost of a single machine	8.10 m [30]
	Unit O&M costs	CNY 70,000/year
	Rated operating temperature	25 °C
	Spectral irradiance	1000 W/m ²
	Temperature coefficient service life	−0.0047 20 year
Energy Storage Batteries	Stand-alone capacity	2 MWh/0.25 MW [37]
	The cost of a single machine	CNY 36,000 [37]
	Unit O&M costs	CNY 1800/year [37]
	Charge efficiency	0.9
	Discharge efficiency	0.9
	service life	10 year [37]
Thermal Power Units	Stand-alone capacity	300 MW
	The cost of a single machine	CNY 1241.535 M [30]
	Unit O&M costs	CNY 600/year [30]
	Flexibility retrofit costs	120/MW
	Climb cap	90 MW/h
	Lower limit of climbing	90 MW/h
	Peak oil shaving and oil consumption	2.3 t/h
	Oil prices	CNY 11,000/t
	Coal consumption coefficient a	0.000381
	Coal consumption coefficient b	0.1586
	Coal consumption coefficient c	20.32
Coal prices Service life	CNY 500/t [30] 20 years	

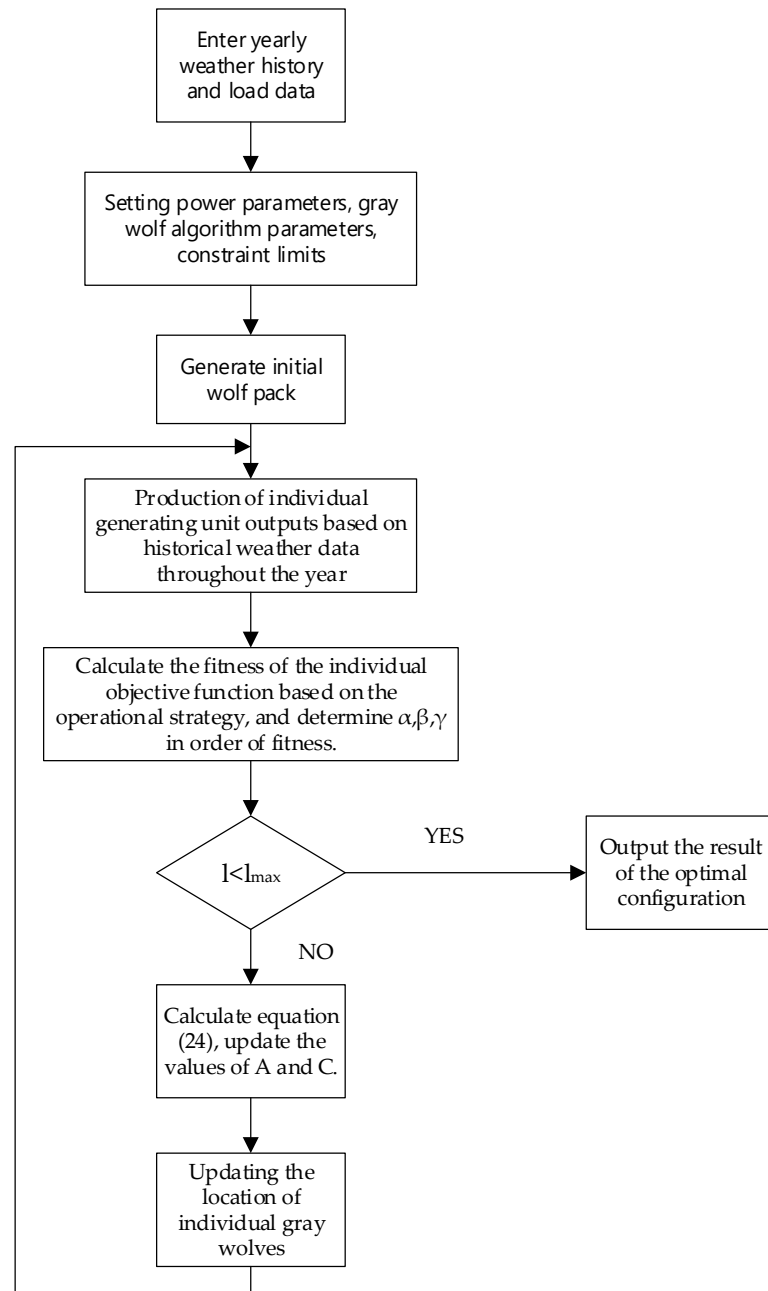


Figure A1. Solution flowchart.

Appendix B

Table A2. Cost composition.

Scenarios	Unit Costs /CNY	O&M Cost /CNY	Peak Shaving Life Cost /CNY	Coal Cost /CNY	Fuel Costs /CNY	Environmental Costs /CNY
1	622.70684 M	31.304 M	42.59063 M	802.51658 M	11.638 M	319.54766 M
2	471.99814 M	63.9696 M	133.84066 M	684.12261 M	40.9607 M	272.40531 M
3	578.78718 M	62.8324 M	105.66714 M	696.48729 M	13.5102 M	277.3287 M

Appendix C

From the configuration result simulation, the total green power generation and discarded power for the whole year are obtained, as shown in Figure A2. Figure A3 shows the

hour-by-hour power deficit throughout the year without considering the participation of the electrolytic aluminum load in the system regulation.

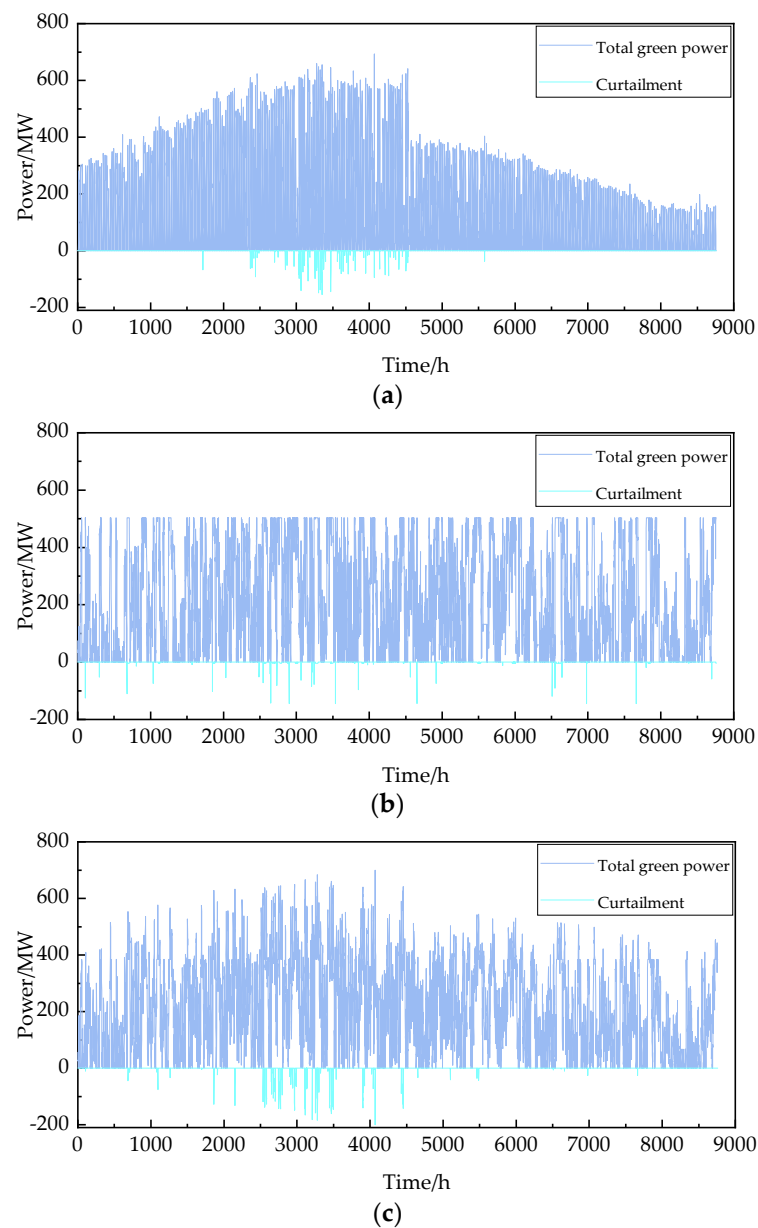


Figure A2. Total green electricity production and curtailment. (a) Total green electricity production and curtailment in Scenario 1. (b) Total green electricity production and curtailment in Scenario 2. (c) Total green electricity production and curtailment in Scenario 3.

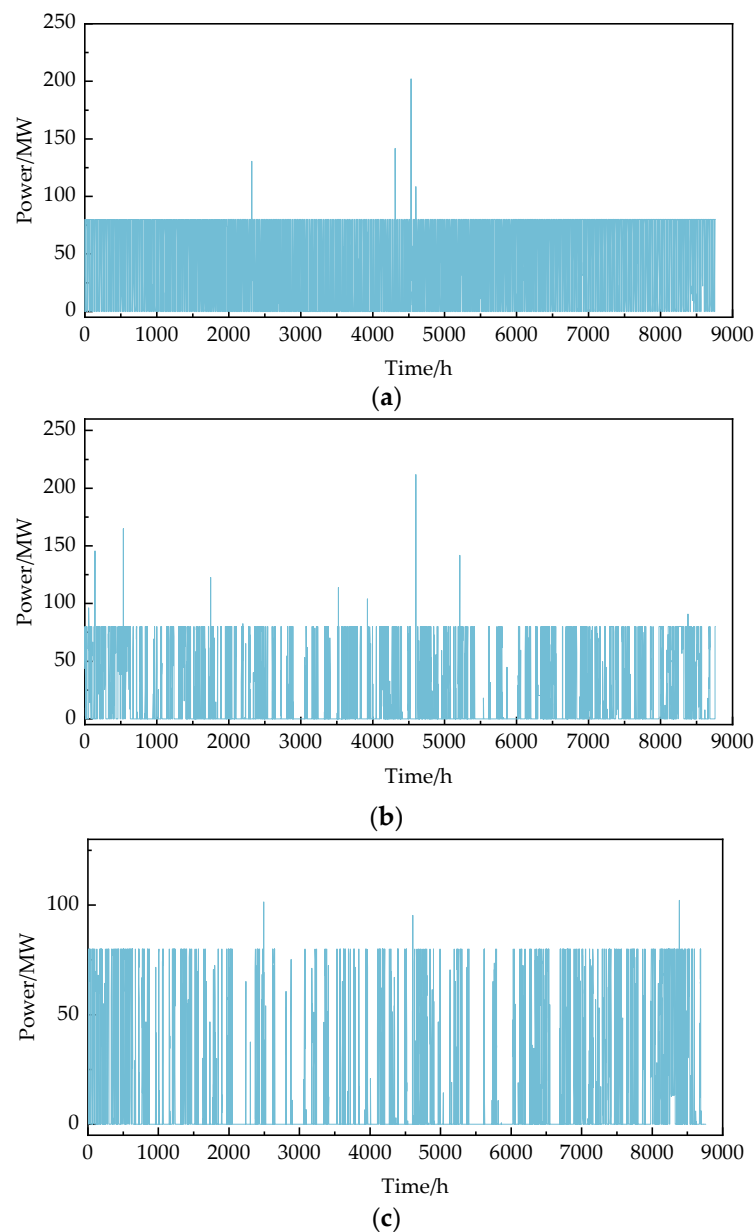


Figure A3. The amount of load adjustment. (a) The amount of load adjustment in Scenario 1. (b) The amount of load adjustment in Scenario 2. (c) The amount of load adjustment in Scenario 3.

Appendix D

Thermal power units will emit exhaust gases during operation, as shown in Table A3.

Table A3. Emission factors and emission benefits.

Types of Exhaust Gases	Emission Factor/t	Emissions Reduction Income per Unit/CNY
CO ₂	0.726	208.5
SO ₂	0.022	1260
NO _x	0.010	2000

References

- Liao, S. *Research on Frequency Control Method of High Energy-Consuming Loads Participating in High Penetration Wind Power Isolated Grid*; Wuhan University: Wuhan, China, 2016.
- Yury, I.; Martirosyan, A. The development of the sodberg electrolyzer electromagnetic field's state monitoring system. *Sci. Rep.* **2024**, *14*, 3501. [[CrossRef](#)] [[PubMed](#)]

3. Zhang, S.; Zhang, Z. Evaluation of the potential of railroad and new energy integration based on photovoltaic power generation. *China Railw.* **2023**, *64*–71. [[CrossRef](#)]
4. He, J.; Yan, N.; Zhang, J.; Chen, L.; Tang, T. Optimization of capacity allocation of photovoltaic energy storage system for electric bus charging station. *J. Cent. South Univ.* **2023**, *30*, 4268–4284. [[CrossRef](#)]
5. Wang, Y.; Liu, D.; Xue, H.; Yu, A.; Tu, Y.; Mi, Y. Multi-objective optimal configuration strategy of optical storage charging station coupled with hydrogen energy. *Power Autom. Equip.* **2023**, *43*, 101–108.
6. Yao, L.; Bai, C.; Fu, H.; Lou, S.; Fu, Y. Optimization of Expressway Microgrid Construction Mode and Capacity Configuration Considering Carbon Trading. *Energies* **2023**, *16*, 6720. [[CrossRef](#)]
7. Wu, H.; Huang, F. Distributed Microgrid Power Planning Based on Hybrid Particle Swarm Algorithm. *East China Electr. Power* **2012**, *40*, 4.
8. Zhang, L.; Xiao, W.; Jiang, C.; Liu, Y.; Li, S.; Zhang, J. Capacity allocation method of key equipment for photovoltaic office buildings. *China Electr. Power* **2024**, *57*, 152–159+169.
9. Zhang, C.; Ran, T.; Li, Z.; Fan, C.; Xia, T.; Yang, Z.; Ding, W. Optimal allocation of independent microgrid capacity based on typical meteorological year and oxygen production time-shiftable load. *Electr. Power Big Data* **2023**, *26*, 13–23.
10. Meng, J.; Lin, Y.; Sun, D.; Qi, Y.; Ma, X.; Guan, Z.; Xie, J. Optimization of wind-hydrogen storage integrated power supply system configuration based on improved SSA. *J. Shanghai Electr. Power Univ.* **2023**, *39*, 557–562.
11. Tian, Y.; Yin, C. Research on capacity optimization of grid-connected microgrid based on improved gray wolf algorithm. *J. Shenyang Eng. Inst. (Nat. Sci. Ed.)* **2023**, *19*, 56–63.
12. Chen, Y.; He, S.; Xie, S.; Hu, B.; Chen, J.; Yuan, Z. Capacity allocation of wind-photovoltaic-hydrogen microgrid based on cooperative game. *J. Sol. Energy* **2024**, *45*, 395–405.
13. Ding, W.; Su, X.; Liao, S.; Tang, Q.; Yang, J. Optimization of photovoltaic energy storage capacity allocation based on Harris Hawk optimization algorithm. *Electron. Des. Eng.* **2024**, *32*, 96–101.
14. Li, C. Optimal allocation of photovoltaic microgrid energy storage capacity based on discrete particle swarm algorithm. *Electro Technol.* **2023**, 93–96. [[CrossRef](#)]
15. Liu, M.; Huo, H.; Han, Z.; Wu, Z. A planning and design method for rural energy systems based on two-layer stochastic optimization. *Renew. Energy* **2023**, *41*, 1675–1684.
16. Wang, Y.; Lu, F.; Li, J.; Tan, Z.; Sun, Z.; Xu, W.; Song, Z.; Liu, Z. Research on planning and allocation of energy system in low carbon park based on comprehensive optimization objective. *China Electric Power.* **2023**, 1–12. Available online: <https://kns.cnki.net/kcms/detail/11.3265.TM.20231121.0931.002.html> (accessed on 21 November 2023).
17. Lu, L.; Yuan, T.; Wang, M.; Li, X.; Li, M.; Pu, Q.; Zhang, X. Configuration and scheduling dual optimization of regional integrated energy systems considering efficiency. *Renew. Energy* **2024**, 1–9. [[CrossRef](#)]
18. Xu, L.; Yang, M.; Wang, X.; Jiang, Q.; Zhang, Z.; Zhu, Y. Two-stage capacity optimization allocation for renewable energy multi-energy complementary system. *J. Nanjing Univ. Technol. (Nat. Sci. Ed.)* **2024**, *46*, 198–204+234.
19. Wang, X.; Chen, Z.; Bian, Z.; Wang, Y.; Wu, Y. Optimal allocation of wind-generation and storage capacity for smart microgrid based on particle swarm optimization algorithm. *Integr. Smart Energy* **2022**, *44*, 7.
20. Abduwaiti, X.; Lv, H.; Chao, Q. Optimal allocation of wind-photovoltaic-hydrogen microgrid capacity based on non-cooperative game. *Jiangsu Electr. Eng.* **2022**, *41*, 110–118.
21. Jin, S.; Fang, F.; Zhu, Z.; Liu, J. Game analysis of microgrid capacity allocation under different investment models taking into account the shortage rate constraint. *China Electr. Power* **2020**, *53*, 9.
22. Engin, M.; Engin, D. Sizing PV-wind hybrid energy system for lighting. *Int. J. Dev. Sustain.* **2012**, *1*, 85–98.
23. Ding, M.; Wang, B.; Zhao, B.; Chen, Z. Optimal capacity allocation of independent wind-diesel-diesel storage microgrid system. *Grid Technol.* **2013**, *37*, 7.
24. Ma, X.; Wu, Y.; Fang, H.; Sun, Y. Optimal allocation of wind/photovoltaic/storage hybrid microgrid power supply using improved bacterial foraging algorithm. *Chin. J. Electr. Eng.* **2011**, *31*, 9.
25. Zhou, J.; Weng, Z.; Song, X. Capacity allocation method for islanded photovoltaic-storage microgrids taking into account reliability and economy. *Power Syst. Autom.* **2021**, *45*, 166–174.
26. Xu, L.; Ruan, X.; Zhang, B.; Mao, C. Improved optimal allocation method for the capacity of wind-solar-storage complementary power generation system. *Chin. J. Electr. Eng.* **2012**, *32*, 11.
27. He, S. *Research on the Optimal Configuration of Industrial Photovoltaic Storage Microgrid Power Capacity and Its photovoltaic Array*; Nanjing Normal University: Nanjing, China, 2018.
28. Xu, J.; Liu, N.; Yu, L.; Lei, J.; Zhang, J. Optimal allocation of industrial photovoltaic microgrid energy storage taking into account important loads. *Power Syst. Prot. Control* **2016**, *44*, 29–37.
29. Jian, X. *Optimal Configuration Method of Battery Energy Storage System for Industrial User-Based Photovoltaic Microgrid*; North China Electric Power University (Beijing): Beijing, China, 2016.
30. Chu, T.; Jiang, M.; Yang, M.; Yan, Z.; Wang, T. Capacity optimization design of wind-solar complementary self-power plant for electrolytic aluminum. *Light Met.* **2022**, 58–62. [[CrossRef](#)]
31. Xu, J.; Liao, S.; Sun, Y.; Ma, X.; Gao, W.; Li, X.; Gu, J.; Dong, J.; Zhou, M. An Isolated Industrial Power System Driven by Wind-Coal Power for Aluminum Productions: A Case Study of Frequency Control. *IEEE Trans. Power Syst.* **2015**, *30*, 471–483. [[CrossRef](#)]
32. Mohan, N.; Undeland, T. *Power Electronics: Converters, Applications, and Design*; John Wiley & Sons: Hoboken, NJ, USA, 2007.

33. Bao, Y. *Research on Leveraging the Flexibility of Industrial Loads for Power System Frequency Operation*; Wuhan University: Wuhan, China, 2019.
34. Zhao, C.; Wang, B.; Sun, Z.; Wang, X. Optimal allocation of independent microgrid capacity based on improved gray wolf algorithm. *J. Sol. Energy* **2022**, *43*, 256–262.
35. Mirjalili, S.; Mirjalili, S.M.; Lewis, A. Grey Wolf Optimizer. *Adv. Eng. Softw.* **2014**, *69*, 46–61. [[CrossRef](#)]
36. Guo, Z.; Liu, R.; Gong, C.; Zhao, L. Improvement research based on gray wolf optimizer. *Comput. Appl. Res.* **2017**, *34*, 3603–3606+3610.
37. Wu, X.; He, M.; He, W.; Li, X.; Wang, P.; Wu, Y. Optimized capacity allocation of wind-photovoltaic-fire-storage bundled outgoing system considering storage lifetime. *Power Syst. Prot. Control* **2023**, *51*, 66–75.

Disclaimer/Publisher’s Note: The statements, opinions and data contained in all publications are solely those of the individual author(s) and contributor(s) and not of MDPI and/or the editor(s). MDPI and/or the editor(s) disclaim responsibility for any injury to people or property resulting from any ideas, methods, instructions or products referred to in the content.